

# Detection of circulating tumor cells *via* an X-ray imaging technique

Sung Yong Jung,<sup>a,b</sup> Sungsook Ahn,<sup>b</sup> Eunseok Seo<sup>b,c</sup> and Sang Joon Lee<sup>a,b,c\*</sup>Received 31 August 2012  
Accepted 27 November 2012

<sup>a</sup>Department of Mechanical Engineering, Pohang University of Science and Technology (POSTECH), San 31, Hyojadong, Pohang 790-784, Republic of Korea, <sup>b</sup>Center for Biofluid and Biomimic Research, POSTECH, San 31, Hyojadong, Pohang 790-784, Republic of Korea, and <sup>c</sup>Division of Integrative Biosciences and Biotechnology, POSTECH, San 31, Hyojadong, Pohang 790-784, Republic of Korea. E-mail: sjlee@postech.ac.kr

Detailed information on the location and the size of tumor cells circulating through lymphatic and blood vessels is useful to cancer diagnosis. Metastasis of cancers to other non-adjacent organs is reported to cause 90% of deaths not from the primary tumors. Therefore, effective detection of circulating tumors cells (CTCs) related to metastasis is emphasized in cancer treatments. With the use of synchrotron X-ray micro-imaging techniques, high-resolution images of individual flowing tumor cells were obtained. Positively charged gold nanoparticles (AuNPs) which were inappropriate for incorporation into human red blood cells were selectively incorporated into tumor cells to enhance the image contrast. This approach enables images of individual cancer cells and temporal movements of CTCs to be captured by the high X-ray absorption efficiency of selectively incorporated AuNPs. This new technology for *in vivo* imaging of CTCs would contribute to improve cancer diagnosis and cancer therapy prognosis.

© 2013 International Union of Crystallography  
Printed in Singapore – all rights reserved

**Keywords:** X-ray imaging; cancer cell; circulating tumor cell; gold nanoparticle.

## 1. Introduction

Precise detection of cancer cells significantly contributes to clinical prognosis and diagnosis of cancer. Metastasis of cancers to other non-adjacent organs is reported to cause 90% of deaths not from the primary tumors (Kaiser, 2010). In particular, dynamic imaging of circulating tumors cells (CTCs), the main cause of metastatic cancers, provides great promise for the prevention of deaths from cancer. A variety of detection methods have been introduced to determine CTCs in the blood samples of patients (Paterlini-Brechot & Benali, 2007). However, these methods have technological limitations in the *in vivo* detection of CTCs. Several non-invasive imaging methods, such as computed tomography and positron emission tomography, have also been used to observe metastatic cancers (Hahn *et al.*, 2011; Kaiser, 2010). Because of limitations in spatial resolution, these techniques can only detect large-scale tumors that have grown significantly (Hahn *et al.*, 2011). High-resolution imaging is one of the most important contributions to the detection of CTCs in blood for the investigation of cancer metastasis. In this point of view, the synchrotron X-ray micro-imaging technique is one of the most suitable imaging modalities to observe both the morphological structure and the transport of cancer cells. With recent advancements in image recording systems, *in vivo* measure-

ments with high spatial (1  $\mu\text{m}$ ) and temporal (1 ms) resolutions are now possible with the effective penetration of hard X-rays (Jamison *et al.*, 2011; Kim & Lee, 2006; Lee *et al.*, 2010; Weon *et al.*, 2006).

Gold nanoparticles (AuNPs) are used to improve the imaging efficiency of cells because of their controlled physical properties, effective bioconjugation and high X-ray absorption (Ahn *et al.*, 2010, 2011*b*; Astolfo *et al.*, 2012; Chien *et al.*, 2012; Frens, 1973; Hainfeld *et al.*, 2006; Menk *et al.*, 2011; Sousa *et al.*, 2010; Thaxton *et al.*, 2005; Turkevich *et al.*, 1951). AuNPs can be functionalized with the use of various ligands (Ahn *et al.*, 2010, 2011*b*; Sousa *et al.*, 2010; Thaxton *et al.*, 2005), and this functionalization results in different AuNP–cell interactions; an example is selective penetration of AuNPs into cells on the basis of the conjugated ligand (Ahn *et al.*, 2011*b*; Verma & Stellacci, 2010). Aside from versatile synthetic control and biosafety (Connor *et al.*, 2005), AuNPs can modulate various photophysical processes such as light absorption, light emission, fluorescence and Mie or Rayleigh scattering, and surface-enhanced Raman scattering (Huang *et al.*, 2007*b*). The enhanced properties of AuNPs in photophysical processes have been employed for an effective cancer detection (Durr *et al.*, 2007; El-Sayed *et al.*, 2005; Huang *et al.*, 2007*a*; Popovtzer *et al.*, 2008; Sokolov *et al.*, 2003). AuNPs also have merits as effective X-ray contrast agents because of their high X-ray

absorption coefficient (Ahn *et al.*, 2010, 2011a,b; Astolfo *et al.*, 2012; Chien *et al.*, 2012; Hainfeld *et al.*, 2006; Menk *et al.*, 2011; Jung *et al.*, 2012).

In this paper, the synchrotron X-ray micro-imaging technique is employed to obtain high-resolution images of CTCs with the use of selective cell penetration characteristics of surface-functionalized AuNPs. Four kinds of AuNPs with different surface properties [thioglycolic acid (SH-CH<sub>2</sub>-COOH) (AuNP 1), 6-thioguanine (SH-C<sub>5</sub>H<sub>4</sub>N<sub>5</sub>) (AuNP 2), 2-mercaptoethanol (SH-CH<sub>2</sub>CH<sub>2</sub>OH) (AuNP 3) and 1-propanthiol (SH-CH<sub>2</sub>CH<sub>2</sub>CH<sub>3</sub>) (AuNP 4)] are incorporated into normal cells [human umbilical vein endothelial cells (HUVEC)] and into cancer cells [MDA-MB-231 (human breast cancer cells), which are representative CTCs] to identify a suitable surface property for the enhancement of X-ray image contrast. This selective incorporation is investigated as a function of cell type and surface characteristics of AuNPs.

## 2. Materials and methods

### 2.1. Surface-modified AuNPs

Gold chloride (III) trihydrate (HAuCl<sub>4</sub>·3H<sub>2</sub>O) was dissolved in de-ionized (DI) Milli-Q water ( $1.0 \times 10^{-3}$  mol L<sup>-1</sup>) under refluxing. Sodium citrate tribasic dihydrate solution in DI water ( $4 \times 10^{-2}$  mol L<sup>-1</sup>) was added to the above solution according to the conventional Turkevich method. Boiling conditions were maintained for a further 15 min after the colour change was completed, followed by cooling at room temperature. The final AuNP solution was dialyzed overnight with a Spectra/Por<sup>®</sup>7 membrane (1000 Da cut) against Milli-Q DI water to remove excess sodium citrate tribasic dihydrate. Thiol ligand was added at the second step. By controlling the mole ratio between the gold ion solution and a reducing agent (sodium citrate tribasic dehydrate) under appropriate reaction conditions (refluxing at around 373 K for 15 min), the average diameter of the AuNPs used in this study was about 20 nm with a relatively narrow size variation. After the size of the AuNPs was determined, the surface properties of the citrate-covered AuNPs (naked AuNPs) were modified: 40 μL of 0.1 M ligand aqueous solutions [thioglycolic acid (SH-CH<sub>2</sub>COOH) (AuNP 1), 6-thioguanine (SH-C<sub>5</sub>H<sub>4</sub>N<sub>5</sub>) (AuNP 2), 2-mercaptoethanol (SH-CH<sub>2</sub>CH<sub>2</sub>OH) (AuNP 3) and 1-propanthiol (SH-CH<sub>2</sub>CH<sub>2</sub>CH<sub>3</sub>) (AuNP 4)] were added to the above aqueous solution and stirred at room temperature or between 323 and 333 K for 6–12 h until the colour change stopped. The obtained AuNP solutions were dialyzed overnight using Spectra/Por<sup>®</sup>7 membrane (1000 Da cut) against Milli-Q water for purification. Detailed synthetic procedures are described by Ahn *et al.* (2010).

### 2.2. Cell preparation

Human breast cancer cells (MDA-MB-231, Invitrogen) were cultured in RPMI (Invitrogen) solution containing 10% fetal bovine serum and 1% penicillin-streptomycin. The cells were cultured in a humidified atmosphere with 5% CO<sub>2</sub> at 310 K. Trypsin (0.25%)–EDTA solution was used to detach

the cells from the culture flask for passing the cells. The MDA-MB-231 cells were washed with Dulbecco's phosphate buffered saline (DPBS) and detached from the flask with trypsin–EDTA solution. The detached cells were then pelleted by slow centrifugation and resuspended in RPMI solution containing 10% fetal bovine serum and 1% penicillin-streptomycin.

### 2.3. Incorporation of gold nanoparticles into the cells

Surface-modified AuNPs were introduced into MDA-MB-231 and HUVEC. The cells were cultured in a T75 flask for 2 d and then treated with the AuNP series for 48 h with 1:1 volume ratio to incorporate the AuNPs into the cells. Thereafter, the cells were fixed with 0.5% glutaraldehyde in DPBS for 20 min at room temperature, and then washed with DPBS and detached from the dish with a scraper. The detached cells were resuspended in DPBS. The samples were loaded in a microcentrifuge tube (Eppendorf), and the cells were pelleted by slow centrifugation. After centrifugation, the supernatant was discarded, and the pellet was observed at the bottom of the tube. This pellet was used for the subsequent analyses. Information on the toxicity of the AuNPs solutions is available from our previous study (Ahn *et al.*, 2011b). Viability assays carried out on the considered cell lines [MDA-MB-231 and HeLa (human cervical adenocarcinoma cells, ATCC) in Ahn *et al.* (2011b)] suggested that the applied AuNP loading protocol had a statistically insignificant impact on cell proliferation. Therefore the AuNPs utilized here can be considered biologically inert.

### 2.4. Scanning electron microscopy (SEM) and energy-dispersive X-ray spectroscopy (EDS)

The samples were mounted on metal stubs and coated with nickel (SC7640 model, Quorum Technology). SEM images were obtained with a XL30SFEG (Philips) SEM (connected to energy-dispersive X-ray spectroscopy) at an acceleration voltage of 20 kV.

### 2.5. Secondary ion-mass spectrometry

Time-of-flight secondary ion-mass spectrometry (SIMS) studies were conducted using a CAMECA spectroscope (Model IMS 6F) provided by the National Center for Nanomaterials Technology (Pohang, Korea). Analysis was performed using a Cs<sup>+</sup> gun with 15 keV gap (Ionoptika Ltd) as a primary ion source (continuous current of 2 nA). Secondary ions were analyzed in a reflection mass spectrometer and detected by a dual microchannel plate assembly operating at 20 kV post-acceleration. Flight times were recorded with a 1 ns time-to-digital converter. The raster size was 25 μm × 25 μm. The area for analysis was 20 μm × 20 μm. Only 12 C and 197 Au ions were detected in this study.

### 2.6. Synchrotron X-ray imaging

Synchrotron X-ray images were captured at beamline BL13W of the Shanghai Synchrotron Radiation Facility (SSRF), People's Republic of China. SSRF is a third-genera-

tion synchrotron source with 200 mA beam current and 3.5 GeV storage energy. Si (111) is used as a monochromator, and the energy resolution ( $\Delta E/E$ ) is less than  $5 \times 10^{-3}$ . The 20 keV monochromatic beam has a physical size of 45 mm (horizontal)  $\times$  5 mm (vertical). Objects were placed approximately 30 m downstream of the source, whereas the detector was placed downstream of the objects at a distance of 30 cm. The size of the X-ray beam illuminating the test sample was adjusted to that of the field of view (FOV) using a slit module to avoid unnecessary exposure of the X-rays on the sample. Aluminium sheets of thickness 5 mm placed upstream of the experimental hutch served to block X-rays when the image receptor was idle. With this approach, both sample and detector are protected from unutilized irradiation reducing the associated radiation dose. The primary X-ray image was converted into a visible image on a thin X-ray scintillator YAG crystal. X-ray images were captured using a CCD camera (PCO, PCO2000) with  $2048 \times 2048$  pixels at 500 ms exposure time. With a  $10\times$  objective lens attached in front of the camera, the FOV was approximately  $1.52 \text{ mm} \times 1.52 \text{ mm}$  in physical dimensions.

### 3. Results and discussion

Cell images of HUVEC and MDA-MB-231 were captured before and after incorporation with SEM, and the results are shown in Fig. 1(a). The incorporation efficiency of Au in a cell in terms of mass fraction (wt%) is detected by EDS connected with SEM in Fig. 1(b). From EDS, elemental analysis was carried out for each AuNP-incorporated cell. To simplify the experiment we used only two elements, Au as the main component of the AuNP and C as the main component of the cells. Owing to the far higher atomic number of Au, the Au wt% in AuNP-incorporated cell systems is relatively higher than the mole ratio. The deviation is caused by the different Au wt% of individual cells used for EDS analysis. As shown in Fig. 1(a), AuNP incorporation does not change the shape and the major status of the cells. Owing to a less effective AuNP consumption, the HUVEC–AuNP 2 system exhibits a rather smooth surface, different from that of the MDA-MB-231–AuNP 2 system. Compared with a less effective incorporation of AuNPs into normal cells (HUVEC), AuNPs are highly incorporated into MDA-MB-231 cancer cells. This phenomenon implies that the membranes of cancerous tissues have greater permeability than those of normal cells (Foster & Schepps, 1981). Cancerous cell membranes exhibit different electrochemical properties and different distributions of electrical charges aside from their greater membrane permeability than normal cells (Cure, 1992). Cancer cells are more negatively charged on their surface. Therefore, cationic particles are bound to the cell surface and are translocated across the plasma membrane in contrast to neutral and negatively charged particles that exhibit less effective cell interaction and internalization (Verma & Stellacci, 2010). Therefore, the positively charged AuNP 2 shows the highest incorporation into MDA-MB-231 cells.

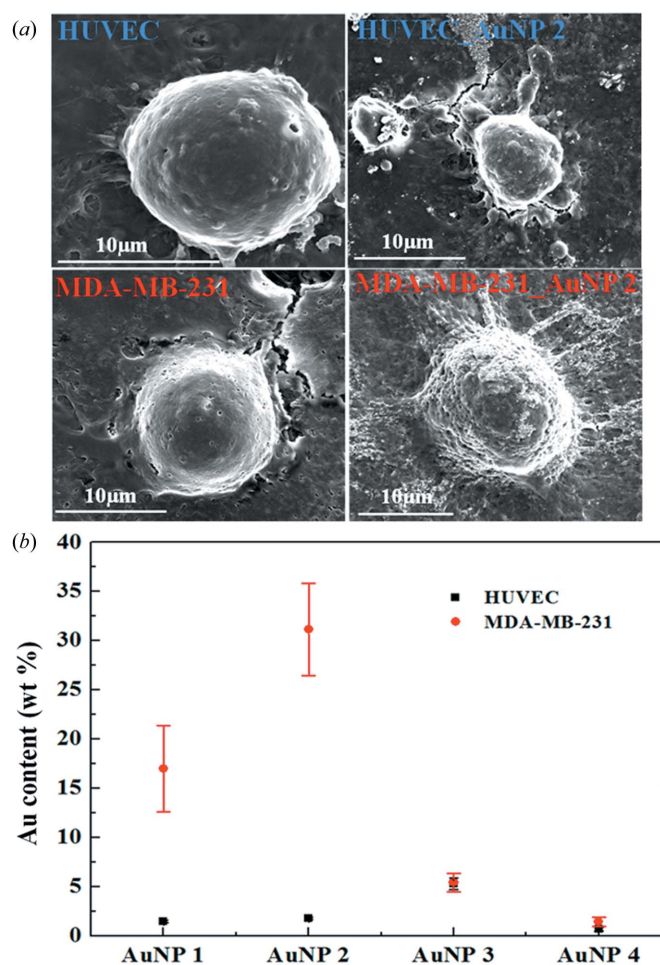


**Figure 1** (a) Typical SEM images. (b) Variation of Au content (wt%) in each AuNP system measured by EDS connected with SEM. The bars represent the standard deviation of Au wt% in individual cells selected for EDS analysis.

The AuNPs that penetrate cells exhibit a marked difference in imaging efficiency compared with those merely attached on the cell surface, especially in the dynamic imaging of moving samples. X-ray absorption is closely related to the density or the number of absorbers and thus to the number of the AuNPs. When AuNPs are only attached on the cell surface, AuNPs located at the two end spots would be the only absorbers. On the contrary, some of the penetrated AuNPs placed in the pathway of the X-ray beam through the cell would work as absorbers. Therefore, the case with penetration accommodates more X-ray absorption. In addition, the AuNPs attached on the cell surface of moving samples are also detached by the forces of ambient flows. The incorporation of AuNPs into cells is very important for the effective imaging of these cells. Quantitative depthwise distribution of AuNPs in a unit cell is obtained *via* secondary ion-mass spectrometry to investigate whether or not AuNPs are attached on the cell surface or whether they penetrate the cell; the results are shown in Fig. 2. Elemental analysis was performed on elements 12C and 197Au. Along the depth of the cell at the

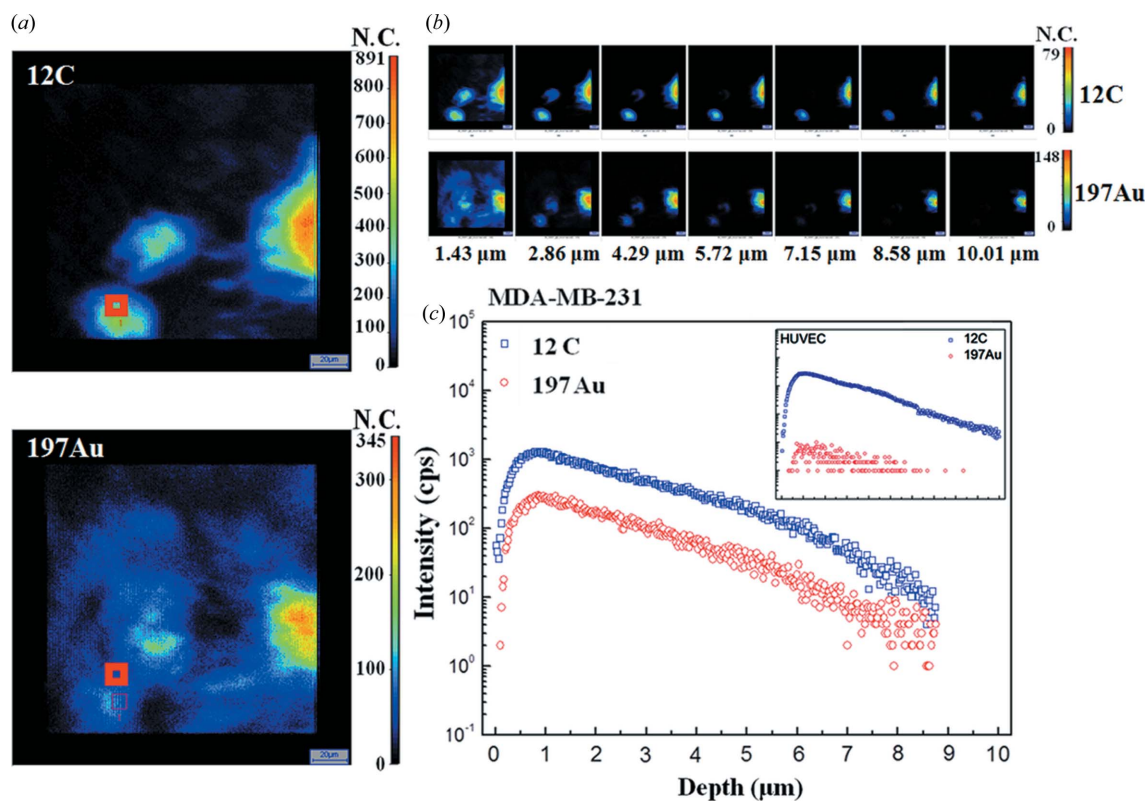


**Figure 2**

(a) SIMS images of the MDA-MB-231–AuNP 2 system. 12 C and 197 Au elements are analyzed. (b) Series of scanned images for C and Au elements. The cell of thickness 10 μm is analyzed from the top to the bottom for seven cycles of runs. (c) Depthwise intensity profiles of C and Au elements at the positions of the squares in (a). The depth profile of the HUVEC–AuNP 2 system is displayed in the upper right corner.

rectangle marked in Fig. 2(a), a series of images for each element is obtained by elemental analysis (Fig. 2b), and the corresponding intensity variations are shown in Fig. 2(c). Au follows C well for the case of MDA-MB-231 but, for the case of HUVEC, only a negligible amount of Au is found. As 12 C is the major constituent element of the cells, elemental analysis of 12 C represents the cell distribution. Spatial distributions of C and Au show that the spatial distribution of AuNPs is well matched with the cell (Fig. 2a). As shown in the depth profiles in Figs. 2(b) and 2(c), AuNPs are not attached on the cell surface but penetrate into the cell in a relatively homogeneous way.

Synchrotron X-ray images of the AuNPs incorporated into cells are shown in Fig. 3(a), and magnified images of the marked square regions are displayed in Fig. 3(b). The spatial resolution of synchrotron X-ray micro-imaging is much higher than that of conventional X-ray imaging methods (Kim & Lee, 2006); thus, AuNPs incorporated into an individual cell are clearly detected. Two different imaging mechanisms based on absorption contrast and phase contrast by which refraction and diffraction fringes are observed are used in the X-ray imaging method. In conventional X-ray imaging with an X-ray tube, absorption contrast is only available because of incoherence of the X-ray source. By contrast, synchrotron X-ray imaging can selectively use both if the two imaging mechanisms vary in sample-to-scintillator distance (Jung *et al.*, 2012). In this study, absorption contrast with refraction fringes is

used through adjustment of the distance to capture X-ray images because the AuNPs incorporated in the cancer cells exhibit a high X-ray absorption rate.

For HUVEC, any image enhancement by X-ray absorption is not observed. Meanwhile, the MDA-MB-231 cancer cells exhibit relatively higher image contrasts compared with the normal HUVEC cells. Depending on the AuNP incorporation efficiency in a cell, the light intensity is different. The boundary between cells is clearly discriminated in the refraction fringes. The MDA-MB-231 cells exhibit high image contrast when AuNP 1 and AuNP 2 are incorporated. This higher image contrast represents more selective incorporation of AuNPs into the cells. In particular, the AuNP 2 system provides clear images of individual cells and the size is about 10 μm. This value is coincident with that of the SEM image in Fig. 1(a).

The light intensity profiles for both cell samples are extracted to compare the image contrasts quantitatively. Variations in X-ray absorption along the dotted lines in Fig. 3(a) are shown in Fig. 3(c). The X-ray absorption of the cancer cell incorporated with AuNP 2 is evidently different from that of normal HUVEC cells. When the image contrast is high, the intensity fluctuations are strong because of a large intensity difference. This result indicates the effective incorporation of AuNPs into the cells. For each cell, intensity profiles are randomly selected along five lines of 500 pixels to compare image contrasts. The intensity fluctuations are

quantitatively evaluated using the following root-mean-square (RMS) value, which is called RMS contrast (Peli, 1990),

$$\text{Intensity fluctuation (RMS contrast)} = \left[ \frac{\sum_N (I_{\text{pix}} - I_{\text{ave}})^2}{N} \right]^{1/2}, \quad (1)$$

where  $I_{\text{ave}}$  is the average value of the intensity profile, and  $I_{\text{pix}}$  represents the intensity at each pixel.  $N$  is the total pixel number in each intensity profile, which is 500 in this study. The level of intensity fluctuations is normalized by  $I_{\text{ave}}$ . In addition to the RMS contrast, we also evaluated the visibility (also

known as the Michelson contrast; Michelson, 1927) commonly used for analyzing patterns in which both bright and dark features are equivalent,

$$\text{Visibility (Michelson contrast)} = \frac{I_{\text{max}} + I_{\text{min}}}{I_{\text{max}} - I_{\text{min}}}, \quad (2)$$

where  $I_{\text{max}}$  and  $I_{\text{min}}$  represent the highest and lowest intensity values, respectively. The results are depicted in Fig. 3(d) and both contrast values are similar. The HUVEC cells show very small contrast levels, whereas the MDA-MB-231 cancer cells exhibit relatively high contrasts. Among the four different

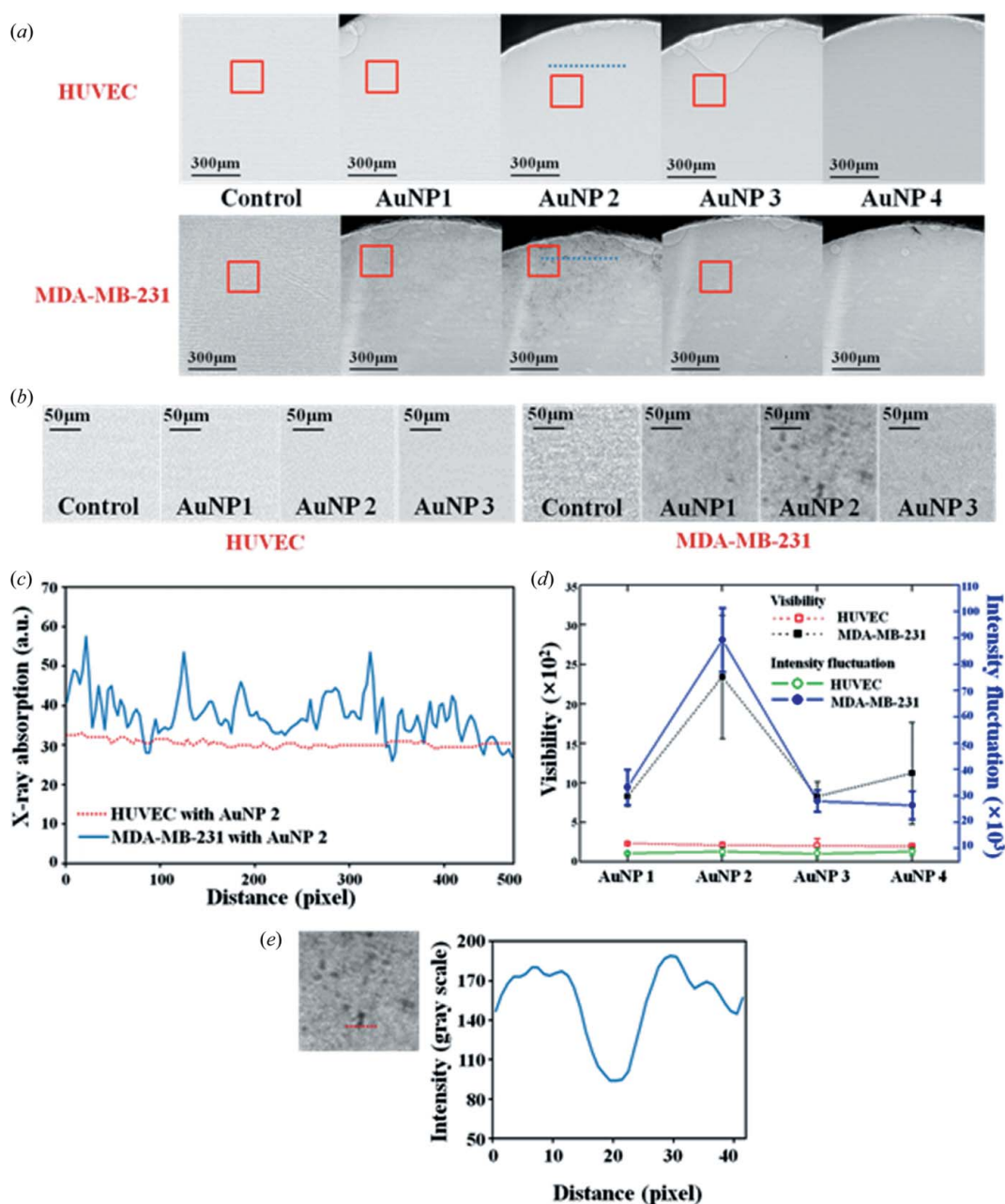


**Figure 3** (a) X-ray images of the HUVEC and MDA-MB-231 systems. (b) Magnified images at the square regions marked in (a). (c) Typical X-ray absorption profiles along the dotted lines for both systems. (d) Variations of visibility (Michelson contrast) and light intensity fluctuation (RMS contrast) normalized by  $I_{\text{ave}}$ . The dotted and solid lines represent the Michelson and RMS contrasts, respectively. (e) Magnified X-ray image of the MDA-MB-231-AuNP2 system and intensity profile along the centreline of a cell (sample 11 in Table 1).

**Table 1**

Cell size, Au concentration and Au amount of each cell tested in this study.

	Sample number									
	1	2	3	4	5	6	7	8	9	10
Size ( $\mu\text{m}$ )	8.9063	8.9063	8.1641	9.6484	9.6484	9.6484	8.1641	8.9063	13.3594	8.9063
Au concentration ( $\text{ng } \mu\text{m}^{-3}$ )	0.6484	0.6039	0.6576	0.6448	0.6205	0.6105	0.6466	0.6430	1.1002	1.0321
Au amount (ng)	0.2398	0.2234	0.1874	0.3032	0.2918	0.2871	0.1842	0.2379	1.3734	0.3818
	11	12	13	14	15	16	17	18	19	20
Size ( $\mu\text{m}$ )	14.8438	8.9063	8.9063	8.1641	14.8438	7.4219	8.1641	8.1641	9.6484	9.6484
Au concentration ( $\text{ng } \mu\text{m}^{-3}$ )	6.2134	0.6502	0.5864	0.3515	2.4729	0.3247	0.8534	0.8163	0.7064	0.6855
Au amount (ng)	10.6403	0.2405	0.2169	0.1001	4.2349	0.0695	0.2432	0.2326	0.3322	0.3224

AuNP systems, AuNP 2 achieves the highest contrast level for MDA-MB-231. With higher incorporation of AuNPs and thus higher gold density the X-ray transmission through a cell decreases, which results in a subsequent increase of the cell contrast against the background. Larger contrast values represent the higher AuNP incorporation efficiency and better imaging performance. The quantitative comparison of contrasts shows that the AuNPs are selectively incorporated according to surface property. MDA-MB-231 cancer cells are clearly observed by the synchrotron X-ray imaging technique with the simple incorporation of AuNPs into the cells.

For MDA-MB-231–AuNP 2, the amount of gold incorporated into the cancer cells was evaluated using the intensity profiles extracted from the corresponding X-ray image. According to the exponential attenuation law, the relationship between the incident and transmitted intensities of the X-ray is expressed as (Cullity, 1978)

$$I = I_0 \exp[-(\mu/\rho)cx], \quad (3)$$

where  $I_0$  and  $I$  are the incident and transmitted intensities of the X-ray, respectively. By assuming the cells to have a spherical shape, the penetration distance  $x$  is evaluated as  $\pi D/4$ . Here, the diameter  $D$  of each cell in the X-ray images is determined as the full width at half-maximum (FWHM). From the magnified X-ray image of the MDA-MB-231–AuNP 2 system, light intensity data along the centreline of individual cells are extracted. A typical intensity profile along the red dotted line is shown in Fig. 3(e). The incident intensity  $I_0$  is obtained by averaging the intensity on the left and right sides of each cell. In addition, the transmitted intensity  $I$  is measured by averaging light intensity values inside the cell. Twenty cells which are clearly distinct from other cells are selected for this evaluation. Because X-rays are almost absorbed by gold, the gold concentration  $c$  can be roughly estimated from the intensity profile using information on the mass attenuation coefficient  $\mu/\rho$  of gold. The  $\mu/\rho$  of gold is  $78.83 \text{ cm}^2 \text{ g}^{-1}$  at 20 keV (Hubbell & Seltzer, 2004). The 20 cell images were evaluated. The size, concentration and amount of gold are summarized in Table 1. The estimated gold concentration is about  $1.038 \times 10^{-3} \text{ ng } \mu\text{m}^{-3}$  and the average size of the cells is  $9.648 \mu\text{m}$ . With an assumption of a spherical-shaped cell, the amount of gold in each cell is evaluated as  $0.488 \text{ ng}$ . The corresponding radiation dose is about  $463 \text{ mGy}$ .

A detailed understanding of the mechanisms of invasion and intravasation of cells (entry of tumor cells into the vasculature) provides the insights needed to prevent the formation of secondary and tertiary metastases. Dynamic imaging of circulating cells is important to understand the invasion process of circulating tumor cells (Condeelis & Segall, 2003). Therefore, MDA-MB-231 cancer cells with positively surface-modified AuNPs are suspended in PBS solution with 10% concentration in volume ratio. The mixture is put into a  $800 \mu\text{m}$  silicon tube using a syringe pump. A schematic diagram of the experimental set-up is shown in Fig. 4(a). The synchrotron X-ray images of the moving cancer cells are captured consecutively, and a typical snapshot is shown in Fig. 4(b). A short video file showing the temporal motion of the cancer cells is available in the supplementary information.<sup>1</sup> Compared with stationary samples, moving samples require a higher image contrast for their dynamic X-ray images to be taken (Ahn *et al.*, 2011b). Fig. 4(b) shows that individual flowing cells in the suspension are clearly observed. This implies that synchrotron X-ray micro-imaging with selective incorporation of AuNPs into CTCs enables the quantitative analysis of moving CTCs with high spatial resolution.

In our previous study, surface-modified AuNPs were incorporated into a human red blood cell (RBC) as a tracer of blood flow (Ahn *et al.*, 2011b). The use of neutral and hydrophilic AuNPs was advantageous in obtaining RBCs reversibly. However, hydrophobic AuNPs were more likely to form aggregations inside the RBCs to increase the imaging efficiency. In this study, the movement of cancer cells is effectively captured with the use of a synchrotron X-ray imaging technique when positively charged AuNPs, which are inappropriate for incorporation into RBCs, are incorporated into the cancer cells. *In vivo* dynamic X-ray imaging of blood flows has become available recently (Jung *et al.*, 2012), and the AuNP-incorporated CTCs are effectively detected by the selective incorporation of AuNPs; these AuNPs are not incorporated into the blood cell but are incorporated exclusively into cancer cells. These results show that the present

<sup>1</sup> Supplementary data for this paper are available from the IUCr electronic archives (Reference: MO5042). Services for accessing these data are described at the back of the journal.

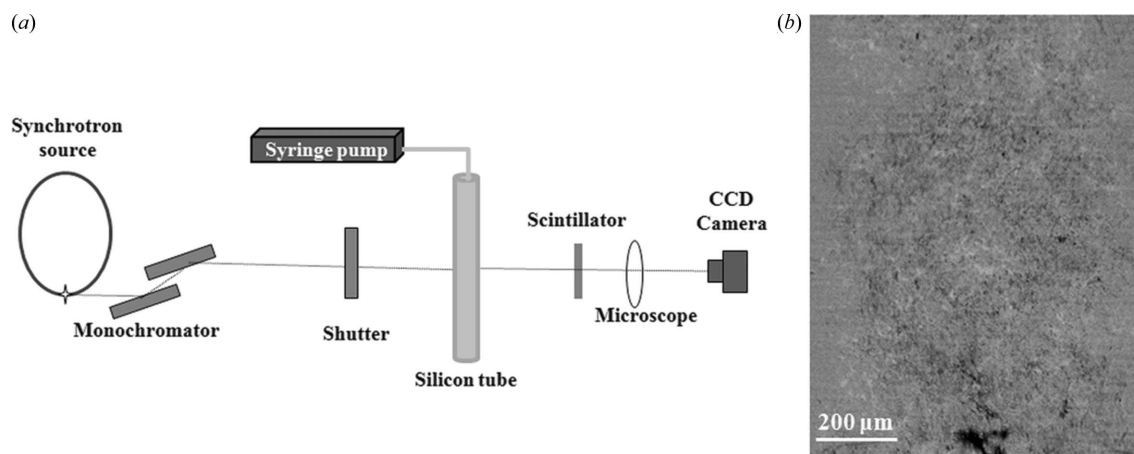


**Figure 4** (a) Schematic diagram of the experimental set-up for investigating the movements of cancer cells. (b) Typical X-ray snapshot image of moving cancer cells (a short video file showing the temporal variation in cell motion is available in the supplementary information).

imaging technique has strong potential to detect cancer cells moving in blood flows.

#### 4. Conclusion

In this study we have demonstrated a high-resolution X-ray imaging technique that enables the quantitative analysis of CTCs moving in blood flows with the selective incorporation of AuNPs. CTCs are closely related to cancer metastasis that causes 90% of deaths not from the primary tumors. Therefore, the ideal treatment of cancer involves diagnosis of the metastasis through quantitative analysis of CTCs and the use of a suitable therapy to remove these CTCs. The X-ray imaging technique with the selective incorporation of AuNPs has strong potential to detect CTCs in blood flows. Even though clinical applications of the synchrotron imaging system are still not fully established, the high-resolution imaging is currently available for *in vivo* imaging of biological samples (Jung *et al.*, 2012; Liu *et al.*, 2008). This technique can contribute to the development of new cancer treatments that eventually prolong lives and improve the quality of life of cancer patients.

This work was supported by the Creative Research Initiatives (Diagnosis of Biofluid Flow Phenomena and Biomimic Research), the WCU program through the National Research Foundation of Korea funded by the Ministry of Education, Science and Technology (R31-2008-000-10105-0) and PAL through the abroad beam time program of the Synchrotron Radiation Facility Project under MEST. This work was performed under the approval of the Shanghai Synchrotron Radiation Facility.

#### References

Ahn, S., Jung, S. Y., Kim, B. H. & Lee, S. J. (2011a). *Acta Biomater.* **7**, 2139–2147.  
 Ahn, S., Jung, S. Y., Lee, J. P., Kim, H. K. & Lee, S. J. (2010). *ACS Nano*, **4**, 3753–3762.  
 Ahn, S., Jung, S. Y., Seo, E. S. & Lee, S. J. (2011b). *Biomaterials*, **32**, 7191–7199.

Astolfo, A., Schültke, E., Menk, R. H., Kirch, R. D., Juurlink, B. H., Hall, C., Harsan, L. A., Stebel, M., Barbeta, D., Tromba, G. & Arfelli, F. (2012). *Nanomedicine*, doi:10.1016/j.naNo.2012.06.004.  
 Chien, C. C., Cheng, C. C., Chen, H. H., Hwu, Y., Chu, Y. S., Petibois, C., Chen, A., Ching, Y. T. & Margaritondo, G. (2012). *Anal. Bioanal. Chem.* **404**, 1287–1296.  
 Condeelis, J. & Segall, J. E. (2003). *Nat. Rev. Cancer*, **3**, 921–930.  
 Connor, E. E., Mwamuka, J., Gole, A., Murphy, C. J. & Wyatt, M. D. (2005). *Small*, **1**, 325–327.  
 Cullity, B. D. (1978). *Elements of X-ray Diffraction*. Reading: Addison-Wesley.  
 Cure, J. C. (1992). *Cancer: An Electrical Phenomenon*. The Human Dimensions Institute.  
 Durr, N. J., Larson, T., Smith, D. K., Korgel, B. A., Sokolov, K. & Ben-Yakar, A. (2007). *Nano Lett.* **7**, 941–945.  
 El-Sayed, I. H., Huang, X. & El-Sayed, M. A. (2005). *Nano Lett.* **5**, 829–834.  
 Foster, K. R. & Schepps, J. L. (1981). *J. Microw. Power*, **16**, 107–119.  
 Frens, G. (1973). *Nat. Phys. Sci.* **241**, 20–22.  
 Hahn, M. A., Singh, A. K., Sharma, P., Brown, S. C. & Moudgil, B. M. (2011). *Anal. Bioanal. Chem.* **399**, 3–27.  
 Hainfeld, J. F., Slatkin, D. N., Focella, T. M. & Smilowitz, H. M. (2006). *Br. J. Radiol.* **79**, 248–253.  
 Huang, X., El-Sayed, I. H., Qian, W. & El-Sayed, M. A. (2007a). *Nano Lett.* **7**, 1591–1597.  
 Huang, X., Jain, P. K., El-Sayed, I. H. & El-Sayed, M. A. (2007b). *Nanomedicine*, **2**, 681–693.  
 Hubbell, J. H. & Seltzer, S. M. (2004). *Tables of X-ray Mass Attenuation Coefficients and Mass Energy – Absorption Coefficients*, Version 1.4. Gaithersburg: National Institute of Standards and Technology.  
 Jamison, R. A., Dubsy, S., Siu, K. K., Hourigan, K. & Fouras, A. (2011). *Ann. Biomed. Eng.* **39**, 1643–1653.  
 Jung, S. Y., Ahn, S., Nam, K. H., Lee, J. P. & Lee, S. J. (2012). *Int. J. Cardiovasc. Imaging*, **28**, 1853–1858.  
 Kaiser, J. (2010). *Science*, **327**, 1072–1074.  
 Kim, G. B. & Lee, S. J. (2006). *Exp. Fluids*, **41**, 195–200.  
 Lee, S. J., Jung, S. Y. & Ahn, S. (2010). *Biosens. Bioelectron.* **25**, 1571–1578.  
 Liu, P., Sun, J., Guan, Y., Yue, W., Xu, L. X., Li, Y., Zhang, G., Hwu, Y., Je, J. H. & Margaritondo, G. (2008). *J. Synchrotron Rad.* **15**, 36–42.  
 Menk, R. H., Schültke, E., Hall, C., Arfelli, F., Astolfo, A., Rigon, L., Round, A., Ataermannan, K., MacDonald, S. R. & Juurlink, B. H. (2011). *Nanomedicine*, **7**, 647–654.  
 Michelson, A. A. (1927). *Studies in Optics*. University of Chicago Press.

- Paterlini-Brechot, P. & Benali, N. L. (2007). *Cancer Lett.* **253**, 180–204.
- Peli, E. (1990). *J. Opt. Soc. Am. A*, **7**, 2032–2040.
- Popovtzer, R., Agrawal, A., Kotov, N. A., Popovtzer, A., Balter, J., Carey, T. E. & Kopelman, R. (2008). *Nano Lett.* **8**, 4593–4596.
- Sokolov, K., Aaron, J., Hsu, B., Nida, D., Gillenwater, A., Follen, M., MacAulay, C., Adler-Storthz, K., Korgel, B., Descour, M., Pasqualini, R., Arap, W., Lam, W. & Richards-Kortum, R. (2003). *Technol. Cancer Res. Treat.* **2**, 491–504.
- Sousa, F., Mandal, S., Garrovo, C., Astolfo, A., Bonifacio, A., Latawiec, D., Menk, R. H., Arfelli, F., Huewel, S., Legname, G., Galla, H. J. & Krol, S. (2010). *Nanoscale*, **2**, 2826–2834.
- Thaxton, C. S., Rosi, N. L. & Mirkin, C. A. (2005). *MRS Bull.* **30**, 376–380.
- Turkevich, J., Stevenson, P. C. & Hillier, J. (1951). *Discuss. Faraday Soc.* **11**, 55–75.
- Verma, A. & Stellacci, F. (2010). *Small*, **6**, 12–21.
- Weon, B. M., Je, J. H., Hwu, Y. & Margaritondo, G. (2006). *Int. J. Nanotechnol.* **3**, 280–297.